Fabrication of photoactive CaTiO$_3$–TiO$_2$ composite thin film electrodes via facile single step aerosol assisted chemical vapor deposition route

Muhammad Ali Ehsan[1] · Rabia Naeem[2] · Vickie McKee[3] · Abdul Rehman[4] · Abbas Saeed Hakeem[1] · Muhammad Mazhar[5]

Abstract

CaTiO$_3$–TiO$_2$ composite oxide films have been employed, for the first time, as photoelectrodes in photoelectrochemical (PEC) splitting of water. The transparent methanol solutions of Ti(^{i}Pro)$_4$ and newly synthesized calcium complex [Ca$_2$(TFA)$_3$(OAc) (^{i}PrOH)(H$_2$O)(THF)$_3$] (1) (where TFA stands for trifluoroacetato; OAc stands for acetate; and ^{i}PrOH stands for isopropanol) were utilized for aerosol assisted chemical vapor deposition (AACVD) of the target films. The composite electrodes were deposited on fluorine doped tin oxide (FTO) coated conducting glass substrates at varying deposition temperatures of 500– 600 °C. The resulting films were extensively characterized by powder X-ray diffraction, X-ray photoelectron spectroscopy, energy dispersive X-ray analysis and scanning electron microscopy. PEC responses of all the composite electrodes were studied under simulated solar irradiation of AM 1.5 G (100 mW cm^{-2}). The CaTiO$_3$–TiO$_2$ photoanode formed at 600 °C showed higher photocurrent density of 610 µA cm^{-2} at 0.7 V versus Ag/AgCl/3 M KCl reference electrode as compared to the other two electrodes fabricated similarly with only difference of fabrication temperature (i.e., 500 and 550 °C).

1 Introduction

Photoelectrochemical (PEC) splitting of water for generating hydrogen is truly believed to be a safe and auspicious route for solar energy conversion. This technology relies on the sun, a long-lasting source of energy, while using ubiquitous water as a renewable energy resource. For the progression of PEC technology, gigantic efforts have been made to develop a robust and stable photocatalyst that can ideally perform water decomposition reaction at milder conditions to produce hydrogen, thus to meet the industrial demands [1–3]. In this regard, titanium dioxide (TiO$_2$) and various other Ti-based oxide semiconductors are extensively researched owing to their significant photocatalytic efficiency while being non-toxic, chemically stable, and low cost [4–6]. Ti-based composites of alkaline earth metal titanates (e.g., CaTiO$_3$, SrTiO$_3$ and BaTiO$_3$) are considered better choices among them in this splitting of water. The main reason of such popularity is their unique perovskite structure [7, 8]. In such perovskite structures, the lowest part of the conduction band is mainly comprised of empty d orbitals of the transition-metal (e.g., Ti^{4+}) having a potential slightly negative than 0 V, which makes them capable of oxidizing water [7]. However, a significant drawback of these perovskite photocatalyts is their limited light absorption capacity which is linked to their poor charge separation efficiency. This is the result of their large band gap and high trapping density [9–11]. Two predominant strategies have been proposed in order to tackle these problems [9, 12].

Firstly, the methods of bandgap engineering have been employed to have a band edge position alignment by the development of heterojunctions or by doping these matereials with metal ions so as to configure these materials

✉ Muhammad Ali Ehsan
meali@kfupm.edu.sa

1 Center of Research Excellence in Nanotechnology (CENT), King Fahd University of Petroleum and Minerals, Dhahran 31261, Saudi Arabia

2 Department of Chemistry, Government College University, Lahore, Pakistan

3 School of Chemical Sciences, Dublin City University, Dublin 9, Glasnevin, Ireland

4 Department of Chemistry, King Fahd University of Petroleum and Minerals, Dhahran 31261, Saudi Arabia

5 Department of Environmental Sciences, Fatima Jinnah Women University, The Mall, Rawalpindi 46000, Pakistan

for spontaneous water splitting [13, 14]. The perovskite based photoanodes modified by this strategy (e.g., SrTiO₃/Cu₂O [15], BaTiO₃/TiO₂ [16], CaTiO₃/Pt [17] have shown enhanced photocatalytic activities, thereby utilizing the solar spectrum more successfully. Secondly, synthetic strategies has been devised to enhance the separation of electron–hole pairs in photoanodes by crystal size reduction to the scale of the hole diffusion lengths and by increasing the carrier conductivity through morphological and crystallographic control. However, both approaches are confined by the limits of the fabrication method.

In this regard, aerosol assisted chemical vapor deposition (AACVD) has shown great promise in engineering the photoelectrodes with novel morphologies, high crystallinity and controlled thickness [18–20]. AACVD is highly effective in constructing bi/multicomponent photoelectrodes with precise elemental stoichiometry and ensures the homogenous coupling of the bi or tri phases in a single step, leading to the reduction of the band gap of the material [14, 21, 22]. The homogeneity and the size of the aerosol droplets can easily be tuned to have a control on the morphology of the resulting films. This is done by controlling the viscosity of the precursor solutions and the frequency of the aerosol generator during the AACVD process [23]. During deposition *via* AACVD, the particle growth and sintering processes simultaneously occur on the substrate surface to develop well interconnected morphological features and produce adhesive film electrodes. This particle–particle or particle–conducting layer connection improves the electrical contacts and hence, the conductivity of the nanoparticle based thin films. The result is the enhanced charge transport properties of the resulting electrodes, thus exhibiting a better photocatalytic performance [24]. The demands of the AACVD technique are less stringent as compared to other film deposition methods; it only requires a metal–organic precursor which should be adequately soluble in any organic solvent.

Recently, we observed that magnesium dititanate (MgTi₂O₅) electrodes produced by AACVD showed enhanced PEC water splitting performance and prolonged electrochemical stability [25] which motivated us to develop and assess the photoelectroactivity of CaTiO₃. Calcium titanate (CaTiO₃), again having a perovskite structure, is actively involved in photocatalytic activities [26]. It has a high reduction potential which is even higher than that of the well-known TiO₂ photocatalyst [27]. This has led to significant recent research devoted to the photocatalytic performances of CaTiO₃ and its doped derivatives either for hydrogen production or photodecomposition of organic molecules [28–30]. Recently a photocatalyst, CaTiO₃/Pt, was designed that demonstrated photocatalytic hydrogen production under a flow of water and methane [17]. The photocatalytic activity of CaTiO₃ toward the degradation of organic pollutants is also well established. Yang et al.

synthesized the nanocomposite of CaTiO₃–graphene and found an improved photocatalytic degradation of methyl orange [31].

Instead of metal titanates, other nanostructured mixed metal oxides have also shown great promise toward photocatalytic applications. Recently, nanostructured YbVO₄ and YbVO₄/CuWO₄ nanocomposites were successfully synthesized using sonochemical method and their behavior towards photo-destruction of methylene blue was evaluated. It has been observed that due to coupling of CuWO₄ into YbVO₄ photocatalytic and optical properties were improved which lead to improve photo-destruction efficiency for methylene blue from 65 to 100%, during 120 min irradiation [32]. In a different study, YbVO₄ and nanocomposite YbVO₄/NiWO₄ in a variety of nano designs and sizes were produced by just changing the polymeric capping agents. The resultant photocatalysts efficiently performed photo-degradation of many organic dyes such as rhodamine B, methylene blue, methyl orange, and phenol red, under visible light [33]. Moreover, different morphologies of novel ZnLaFe₂O₄/NiTiO₃ nanocomposites were fabricated by using different surfactant agents such as cetrimonium bromide, sodium dodecyl sulfate, polyvinylpyrrolidone, polyvinyl alcohol, and oleic acid through a polyol assistant sol–gel method. This nanocomposite have antibacterial activity against Gram-negative *Escherchia coli* (ATCC 10536) and Gram-positive *Staphylococcus aureus* (ATCC 29737). Antibacterial results demonstrate that nanocomposite significantly reduced the growth rate of *E. coli* bacteria and *S. aureus* after 120 min [34].

Furthermore, the literature suggests that it is interesting to improve the photocatalytic performance of CaTiO₃–TiO₂ composite, which has not been investigated for PEC water splitting so far. Herein, we report the fabrication of CaTiO₃–TiO₂ electrodes by vaporizing a homogenous mixture of a self-designed Ca-precursor [Ca₂(TFA)₃(OAc)(*i*PrOH)(H₂O)(THF)₃] and commercially available Ti(*i*Pro)₄ in methanol under AACVD conditions. The deposition of CaTiO₃–TiO₂ was conducted at three different temperatures of 500, 550 and 600 °C on fluorine doped tin oxide (FTO) coated conducting substrates in air atmosphere. The composite oxide films were investigated by XRD, SEM, EDX, XPS, and UV–Vis spectrophotometry. Moreover, the PEC properties of CaTiO₃–TiO₂ films were also examined in order to evaluate their performance toward photocatalytic water splitting applications.

2 Experimental

2.1 Materials and methods

All the reagents and chemicals were supplied by Sigma-Aldrich. All the chemicals were used as received except

tetrahydrofuran which was rigorously dried over sodium benzophenoate and was distilled immediately before use. All the synthetic work was carried out in Schlenk tubes fitted with the vacuum lines using hot plates for temperature control and dry argon for an inert atmosphere. The controlled thermal analyses were performed on a Perkin Elmer TGA 4000 thermogravimetric analyzer equipped with a computer interface. These high temperature measurements were carried out in ceramic crucibles under an inert atmosphere of flowing nitrogen (flow rate = 25 mL min^{-1}) with a temperature ramping of 10 °C min^{-1}. The melting point determinations were made in a capillary tube using an electrothermal apparatus from Mitamura Riken Kogyo (Japan) Model: MP.D. Fourier transform infra-red (FT-IR) spectra were recorded using a single reflectance ATR instrument (4000–450 cm^{-1}, resolution 4 cm^{-1}). NMR spectra were obtained using a JEOL DELTA2 NMR spectrometer. These experiments were performed at field strength of 400 MHz in Methanol-D4 used as the solvent.

2.2 Synthesis of [Ca$_2$(TFA)$_3$(OAc)(^{i}ProH)(H$_2$O)(THF)$_3$] (1)

In an effort to synthesize a heterobimetallic Ca–Ti complex, a mixture of Ca(OAc)$_2$·2H$_2$O (0.5 g, 2.63 mmol), Ti(^{i}Pro)$_4$ (1.55 mL, 5.26 mmol) and trifluoroacetic acid (0.58 mL, 7.90 mmol) in 20 mL THF was stirred for 2 h in a schlenk tube under an inert atmosphere of dry argon.

The reaction mixture was evaporated under vacuum which resulted into a white powder. This material was re-dissolved in THF. The transparent solution so obtained was cannula-filtered and placed overnight at room temperature to obtain colourless block shaped crystals of complex (**1**) (75% yield).

Mp: 220 °C (decomposition). ^{1}H NMR (MeOH): δ = 3.87 ppm [m, H, CH] (^{i}PrOH), δ = 3.68 [t, 12H, OCH$_2$] (THF), δ = 2.12 [s, 1H, OH] (^{i}PrOH), δ = 1.12 ppm [d, 6H, CH$_3$] (^{i}PrOH), δ = 1.83 ppm [s, 12H, CH$_2$] (THF), δ = 1.96 ppm [s, 3H, CH$_3$] (OAc), ^{19}F NMR (MeOH): δ = − 76.94 ppm [s, 9F, CF$_3$]. IR: ν_{max}/cm^{-1} 3326br, 2983w, 2886w, 1665s, 1452s, 1194s, 1141s, 1038s, 884s, 796s, 719s, 652s, 607s, 520w, 463w. TGA: 70–120 °C (3.0 wt% loss); 135–235 °C (28.0 wt% loss); 238–500 °C (51.0 wt% loss), (Residual mass of 18.0%); (Cal. for CaO ≈ 15.0%). All characterization and analysis results are summarized in Table 1.

2.3 Single-crystal X-ray crystallographic analyses

Single crystal X-ray data was collected at 150 (2) K on a Synergy, Dualflex, AtlasS2 diffractometer using CuK$_\alpha$ radiation (λ = 1.54184 Å) and was corrected for the effects of Lorentz-polarization and absorption. Using ShelXle [35], the structure of the resulting crystals was solved and refined by dual space methods (SHELXT) [36] as an inversion twin, on F^2 using all the reflections (SHELXL-2014) [37]. During the refinement process, all non-hydrogen atoms were refined by anisotropic atomic displacement parameters whereas the hydrogen atoms were inserted at calculated positions using a riding model. The only exception was the hydrogen atoms coordinated with water molecule, which were located from difference maps and their coordinates were refined. The CF$_3$ groups on two of the CF3COO$^-$ ions were disordered and modelled using two positions related by rotation; one of the uncoordinated THF molecules was also modelled as disordered over two overlapping conformations. All these parameters of data collection and refinement are briefly described in Table 2. CCDC 1531480 contains the supplementary crystallographic data for this work. These data can be obtained free of charge from The Cambridge Crystallographic Data Centre via http://www.ccdc.cam.ac.uk/data_request/cif.

Table 1 Analysis and characterization of complex [Ca$_2$(TFA)$_3$(OAc)(^{i}PrOH)(H$_2$O)(THF)$_3$] (**1**)

Single crystal analysis	^{1}H-NMR (ppm)	^{19}F-NMR (ppm)	IR (cm^{-1})	TGA temp. versus wt% loss
Determination of chemical formula C$_{15}$H$_{21}$Ca$_2$F$_9$O$_{11}$·2(C$_4$H$_8$O)	δ = 3.87 [m, H, CH] (^{i}PrOH) δ = 2.12 [s, 1H, OH] (^{i}PrOH) δ = 1.12 [d, 6H, CH$_3$] (^{i}PrOH) δ = 3.68 [t, 12H, OCH$_2$] (THF) δ = 1.83 ppm [s, 12H, CH$_2$] (THF) δ = 1.96 ppm [s, 3H, CH$_3$] (OAc)	δ = − 76.94 [s, 9F, CF$_3$]	3326 (O–H) 2983, 2886 (C–H of ^{i}PrOH) 1665, 1452 (C=O of CF3COO$^-$) 1538, 1370 (C=O of CH3COO$^-$) 1194 (C–F) 1141 (C–O)	1st step : 70–120 °C (3.0 wt% loss) 2nd step: 135–235 °C (28.0 wt% loss) 3rd step: 238–500 °C (51.0 wt% loss) Residual mass of 18.0% = CaO

Table 2 Crystal data and refinement parameters for $[Ca_2(TFA)_3(OAc)$ $(^iPrOH)(H_2O)(THF)_3]$ (**1**)

Crystal data	
Chemical formula	$C_{15}H_{21}Ca_2F_9O_{11}\cdot2(C_4H_8O)$
M_r	772.68
Crystal system, space group	Orthorhombic, $P2_12_12_1$
Temperature (K)	150
a, b, c (Å)	13.4102 (3), 15.5099 (4), 16.8614 (4)
V (Å^3)	3507.02 (15)
Z	4
Radiation type	Cu $K\alpha$
μ (mm^{-1})	3.78
Crystal size (mm)	$0.20\times0.18\times0.11$
T_{min}, T_{max}	0.512, 0.698
No. of measured, independent and observed $[I>2\sigma(I)]$ reflections	20,406, 7209, 6359
R_{int}	0.037
$(\sin\theta/\lambda)_{max}$ (Å^{-1})	0.631
$R[F^2>2\sigma(F^2)]$, $wR(F^2)$, S	0.050, 0.148, 1.07
No. of reflections	7209
No. of parameters	531
No. of restraints	1219
$\Delta\rangle_{max}$, $\Delta\rangle_{min}$ (e Å^{-3})	1.44, -0.38
Absolute structure parameter	0.278 (13)

2.4 Thin film fabrication by AACVD

1:1 ratio $CaTiO_3$:TiO_2 composite oxides films were grown on commercially available FTO glass substrates having a resistivity of 8 Ω sq^{-1} using in-house built setup for aerosol-assisted chemical vapour deposition. The substrates with lateral dimensions 1×2 cm^2 were ultrasonically and sequentially cleaned with doubly distilled water, acetone and propan-2-ol, and stored in ethanol until further steps. When ready, the substrate slides were removed from ethanol and air dried before being transferred to the combustion chamber of AACVD (CARBOLITE, Model No. 10/25/130) (6"L×1"D). The substrates were then heated to the desired deposition temperature and kept at the same temperature for 10 min to get the thermal equilibrium. The AACVD setup is illustrated in Scheme 1.

During a typical deposition experiment, a homogeneous mixture of Ca-precursor $[Ca_2(TFA)_3(OAc)(^iPrOH)(H_2O)(THF)_3]$ (0.5 g, 0.65 mmol) and titanium(IV) isopropoxide (0.06 mL, 0.22 mmol) was prepared in 15 mL methanol as solvent. This mixture was utilized for the fabrication of $CaTiO_3$–TiO_2 composite thin films at three different temperatures of 500, 550 and 600 °C. The deposition experiments were continued for a fixed time period of 60 min at each temperature. Thin film deposition parameters are listed in Table 3. Visual examination indicated that films were white, uniform and adhered strongly to FTO substrate as confirmed by the "Scotch tape test".

Scheme 1 Schematic illustration of AACVD setup used for synthesis of $CaTiO_3$–TiO_2 composite films
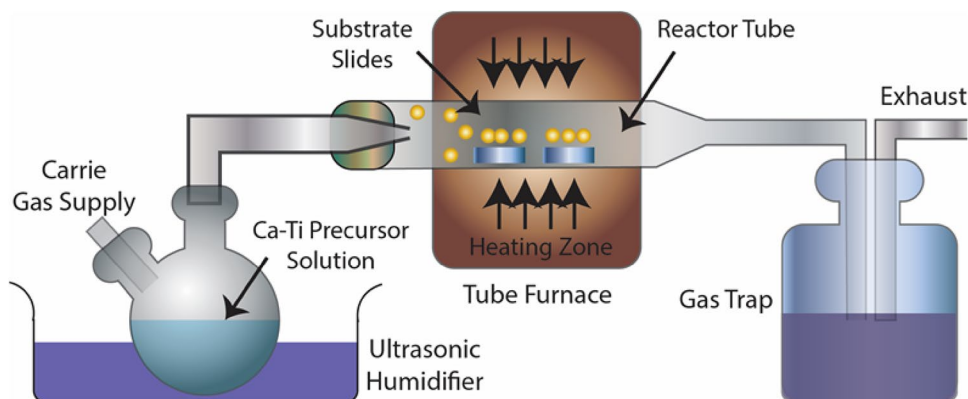
Table 3 Thin films deposition parameters involved in AACVD synthesis of $CaTiO_3$–TiO_2 composite film

Deposition temperatures (°C)	Concentration of precursors Ca-complex + Ti(^{i}Pro)$_4$	Solvent (mL)	Deposition time (min)	Substrate	Carrier gas (mL min^{-1})	Resultant material
500	(0.5 g, 0.65 mmol) + (0.06 mL, 0.22 mmol)	MeOH (15)	60	FTO	150	$CaTiO_3$–TiO_2
550	(0.5 g, 0.65 mmol) + (0.06 mL, 0.22 mmol)	MeOH (15)	60	FTO	150	$CaTiO_3$–TiO_2
600	(0.5 g, 0.65 mmol) + (0.06 mL, 0.22 mmol)	MeOH (15)	60	FTO	150	$CaTiO_3$–TiO_2

2.5 Thin film characterization

The UV–Vis absorption spectra of the thin films were recorded on a Lambda 35 Perkin-Elmer spectrophotometer in the wavelength range of 300–900 nm. Film thicknesses were measured by using a KLA Tencore P-6 surface profiler. In order to verify the crystallinity of the formed composite oxide, the films were examined by X-ray powder diffraction (XRD) using a PANanalytical, X'Pert HighScore diffractometer with primary monochromatic high intensity CuK_{α} ($\lambda = 1.5418$ Å) radiation. Energy dispersive X-ray (EDX, INCA Energy 200, Oxford Inst.) spectroscopy was also carried out in order to determine the metallic ratio of Ca/Ti in the composite. The microstructure of the thin films were investigated using a Lyra 3 Tescan, field emission gun (FEG)-SEM at an accelerating voltage of 5 kV and a working distance of 10 mm. X-ray photoelectron spectroscopy (XPS) was undertaken using an ULVAC-PHI Quantera II instrument with a 32-channel Spherical Capacitor Energy Analyzer under vacuum pressure of 1×10^{-6} Pa using Monochromated Al Kα radiation (1486.8 eV) and natural energy width of 680 meV. The carbonaceous C 1s line (284.6 eV) was used as a reference to calibrate the binding energies.

2.6 Photoelectrochemical measurements

The photoelectrochemical responses of the resulting $CaTiO_3$–TiO_2 composite electrodes were measured using a conventional three-electrode cell configuration on a source of external potential bias (Princeton Applied Research PAR-VersaSTAT-3). Current–voltage characteristics were observed using the linear sweep voltammetry (LSV) technique for a potential range of -0.5 to $+1.2$ V at a scan rate of 10 mV s^{-1}. The $CaTiO_3$–TiO_2 thin films were used as the working electrode in these experiments while having platinum wire as a counter electrode and Ag/AgCl reference electrode. The working electrodes (i.e., $CaTiO_3$–TiO_2 thin films) were dipped into 1 M NaOH electrolyte solutions for the calculations of the photocurrent, and irradiated with a 100 mW xenon lamp (Newport, Model 69907) containing a simulated AM 1.5 G filter as a light source, during the whole length of the experiment.

3 Results and discussion

3.1 An insight into complex (1)

A polymeric complex of calcium $[Ca_2(TFA)_3(OAc)(^iPrOH)(H_2O)(THF)_3]$ (**1**) (TFA = triflouroacetato; OAc = acetato; ^iPro = isopropoxy) has been obtained as a result of our efforts to synthesize a heterobimetallic Ca–Ti complex. The reactants $Ca(OAc)_2 \cdot 2H_2O$ and $Ti(^iPro)_4$ were mixed in the molar ratio of 1:2 in tetrahydrofuran solvent followed by subsequent addition of trifluoroacetic acid with the aim of achieving a Ca–Ti bimetallic compound to be implemented in AACVD for the fabrication of $CaTiO_3$–TiO_2 composite oxide photoelectrodes for PEC water splitting. The synthetic pathway did not successfully produce our desired Ca–Ti bimetallic complex, but instead produced complex (**1**) which was still interesting with regard to AACVD application. Hence we utilized a homogenous methanolic solution of complex (**1**) and $Ti(^iPro)_4$ to fabricate $CaTiO_3$–TiO_2 oxide thin film electrodes. The complex (**1**) was produced in the form of transparent white crystals having a 75% yield. The obtained crystals were quite stable towards air and moisture while exhibiting appreciable solubility in routinely used organic solvents such as methanol, ethanol and acetonitrile etc. The structural composition of the formed complex (**1**) was initially established by single crystal XRD and was further ascertained by AT-IR, ^{1}H and ^{19}F NMR and thermogravimetry analyses. The IR spectra of complex (**1**) indicates that different functional moieties are attached to the calcium centers in (**1**). At 3326 cm^{-1}, a broad peak corresponding to OH functional group is present and at 2983 and 2886 cm^{-1}, there are peaks to indicate the CH group of isopropanol [38]. The symmetric and asymmetric υ(C=O) absorption signals of the acetato and trifluoroacetato ligands have also been observed at 1538 and 1370 cm^{-1} and 1665 and 1452 cm^{-1} respectively. The difference of 168 and 213 cm^{-1} between these symmetric and asymmetric υ(C=O) vibrations reveals the bidentate characteristics of the carboxylate groups of the acetato and trifluoroacetato groups that are coordinated to different calcium atoms [39]. In addition, the peaks at 1194 and 1141 cm^{-1} authenticates the occurrence of C–F and C–O bonds in complex (**1**). ^{1}H-NMR spectra measured from D-methanol solution displays three signals at, $\delta = 3.87$ ppm [p, 4H, CH] $\delta = 2.12$ ppm [s, 1H, OH]and 1.12 ppm [d, 6H, CH$_3$] due to the isopropanol. While two signals at $\delta = 3.68$ ppm [t, 12H, OCH$_2$] and $\delta = 1.83$ ppm [t, 12H, CH$_2$] are for the solvated THF and $\delta = 1.96$ ppm [s, 3H, CH$_3$] are for the acetato groups. Further, the ^{19}F-NMR spectra recorded in methanol displays a singlet at $\delta = -76.94$ ppm [s, 9F, CF$_3$] suggesting the presence of a trifluoroacetato moiety in the formed complex (**1**).

3.2 Description of molecular structure of complex (1)

The asymmetric unit contains two independent calcium ions linked by bridging acetate and trifluoroacetate groups as shown in Fig. 1. Ca^{2+} and Ti^{4+} are isoelectronic, so cannot be readily distinguished only on the basis of X-ray data. However, the M–O bond length data with related assemblies in the CSD (V5.37 and updates) support assignment as Ca^{2+} and are inconsistent with Ti^{4+}
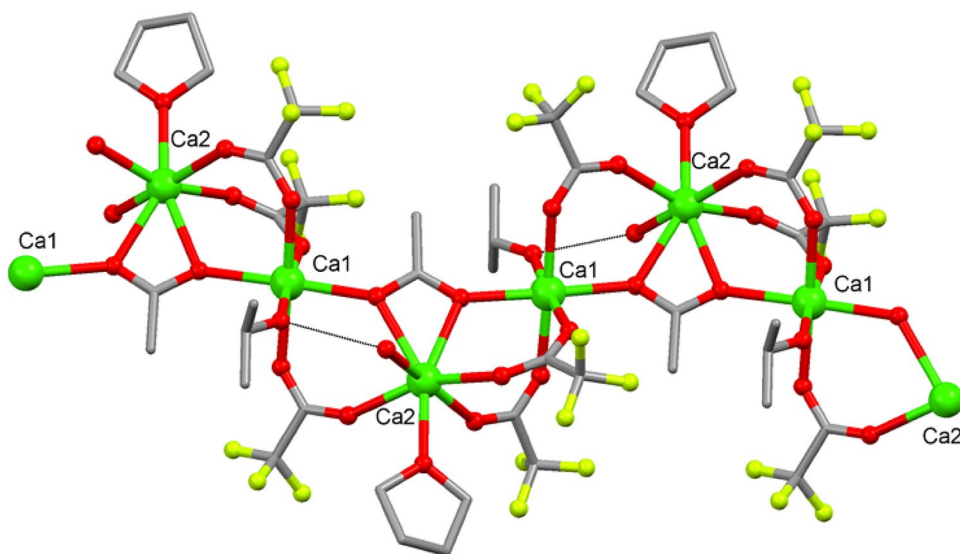
Table 4 Hydrogen-bond geometry (Å, °) for $[Ca_2(TFA)_3(OAc)(^iPro)(H_2O)(THF)_3]$

D–H…A	D–H	H…A	D…A	D–H…A
O1–H2…O71	0.82 (8)	1.88 (8)	2.683 (6)	169 (8)
O1–H1…O81	0.86 (8)	1.92 (8)	2.718 (14)	155 (7)
O1–H1…O81′	0.86 (8)	1.81 (8)	2.628 (13)	159 (7)
O51–H51A…O1^i	0.84	2.07	2.902 (6)	179

Symmetry code: (i) $x - 1/2, -y + 3/2, -z + 1$

[40]. Furthermore, replacing even one of the Ca^{2+} ions with Ti^{4+} would present difficulties with charge balance, since there is only one ionisable proton remaining in the asymmetric unit (on the isopropanol).

The two calcium ions are linked on one side by two *syn* bridging bidentate CF_3COO^- ions and by a single atom bridge from the acetate ligand; on the other by one *syn* bidentate CF_3COO^- ion and a single oxygen donor from the acetate ligand. The acetate ligand acts as a *syn* bidentate ligand to Ca2 and as an anti bidentate bridge linking Ca1 to a symmetry equivalent atom (under synmmetry operation $x - 1/2, -y + 3/2, -z + 1$). Ca1 is 6-coordinate, the coordination sphere completed by an isopropanol ligand while Ca2 is 7-coordinate, having water and THF ligands. Between the coordinated alcohol on Ca1 and the water molecule on Ca2 (under $x - 1/2, -y + 3/2, -z + 1$), an intramolecular hydrogen bond is located whereas two hydrogen bonds are directed from the coordinated water molecule, one to each of the uncoordinated THF molecules (Table 4).

3.3 Pyrolysis of complex (1)

Simultaneous thermogravimetric analysis (TGA) and derivative thermogravimetric (DTG) analyses were performed under a flowing dinitrogen atmosphere (flow rate $= 25$ cm^3 min^{-1}) and with a temperature ramping of 10 °C min^{-1} in order to investigate the thermal stability of complex (**1**). The thermogram thus obtained (Fig. 2) illustrates that the decomposition of (**1**) proceeds into three discrete stages with a continuous weight loss of 3.0%, 28.0% and 51.0%, with the maximum heat intake steps at 98 °C, 220 °C and 272 °C, respectively. At 600 °C, the amount of the residue obtained is ~ 18.0%, which suggest the formation of "*n*" moles of CaO (calculated percentage ≈ 15.0%). Further heating of the residue up to 800 °C bring no significant change in mass, indicating complete decomposition of complex (**1**) yielding a stable residue of CaO. Quantitative pyrolysis of complex (**1**) has been indicated in the equation below, based on TGA information:

$$\left[Ca_2(TFA)_3(OAc)(^iPrOH)(H_2O)(THF)_3\right]_n \xrightarrow{600\,°C} n\{CaO + \text{volatiles}\}$$

3.4 XRD analysis

Figure 3 shows the XRD patterns of the films of $CaTiO_3$–TiO_2 composite formed at three different temperatures. The qualitative phase analysis via XRD indicates the formation of "perovskite $CaTiO_3$" ICSD (98-003-7263) and anatase TiO_2 (ICSD $= 98$-000-9853) phases in all the composite oxide films. The diffraction peaks indicated by (X) at $2\theta = 23.2°, 32.9°, 33.0°, 33.3°, 39.0°, 39.1°, 40.6°, 41.0°, 47.4°, 47.5°, 58.8°, 59.0°, 59.2°, 59.3°, 68.9°, 69.4°,$

Fig. 2 TGA (black) and DTG (dotted red) profiles indicating pyrolysis of complex (**1**) against the increasing temperature under an inert nitrogen atmosphere and temperature ramping of 10 °C min^{-1}. (Color figure online)

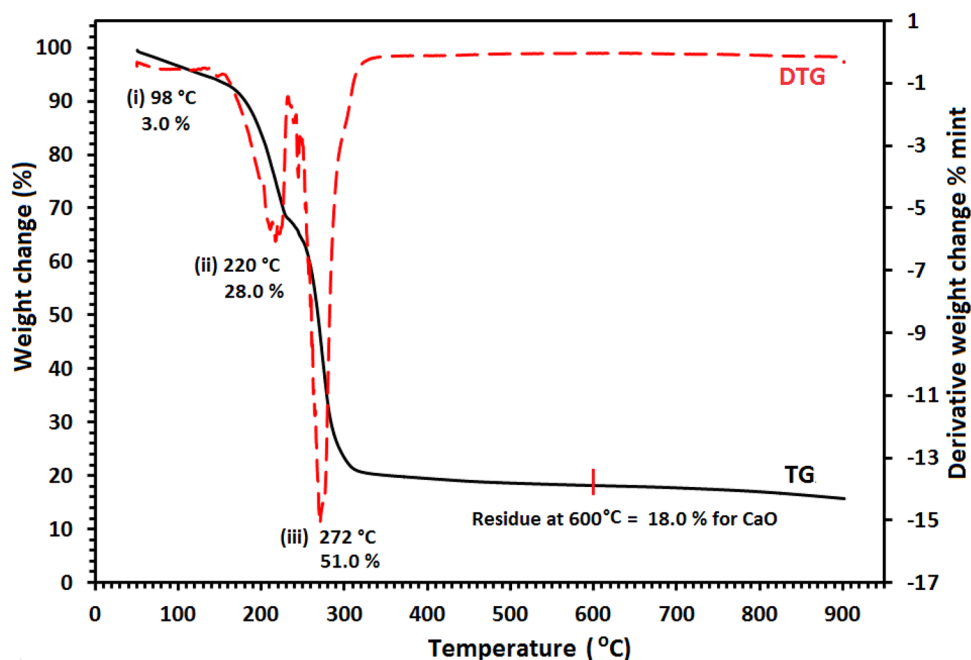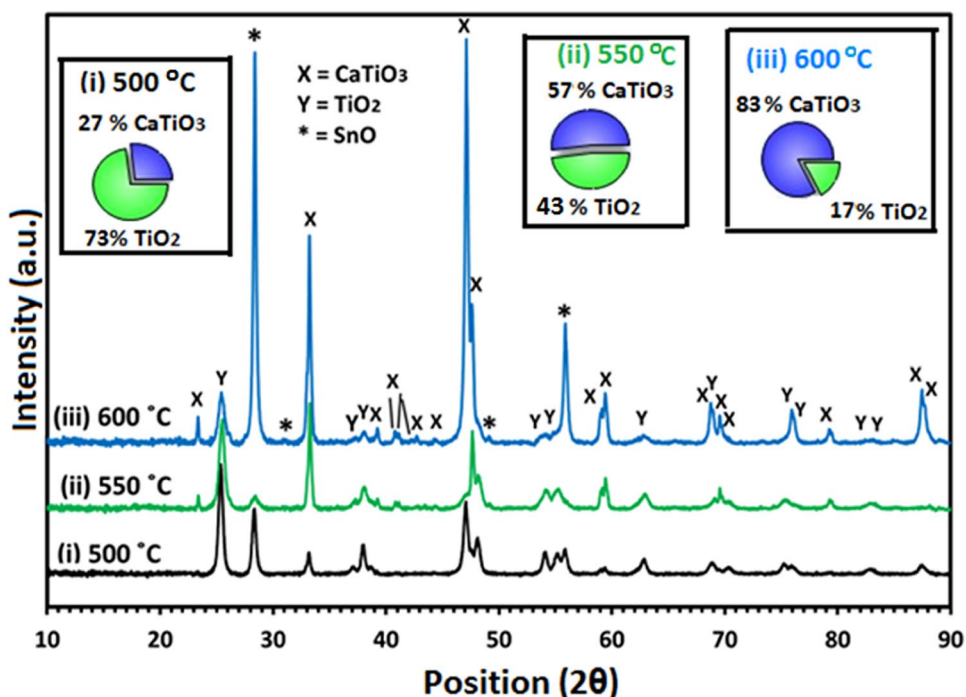**Fig. 3** XRD peak patterns of CaTiO$_3$–TiO$_2$ composite oxide films deposited on FTO glass substrates at different temperatures via AACVD. Insets in the figure shows the crystalline proportion of the phases involved in composite films at (i) 500 °C; TiO$_2$ (73%) and CaTiO$_3$ (27%) (ii) 550 °C; TiO$_2$ (43%) and CaTiO$_3$ (57%) and (iii) 600 °C; TiO$_2$ (17%) and CaTiO$_3$ (83%)

79.0°, 79.2°, 88.0° and 88.9° correspond to the (101), (200), (121), (002), (031), (112), (220), (022), (202), (040), (321), (240), (042), (123), (400), (242), (323), (161), (440), (044) planes, respectively, in good agreement with the orthorhombic CaTiO$_3$ (Fig. 3). The peaks labelled as (Y) at 2θ = 25.2° (011), 36.9° (013), 37.7° (004), 38.5° (112), 48.0° (020), 53.8° (015), 55.0° (121), 62.6° (024), 68.6° (116), 70.2° (220), 75.0° (125) and 82.5° (224) are regarded as the attributive indicator of TiO$_2$ in the tetragonal anatase phase (ICSD = 98-000-9853). The Peaks indicated by (*) are diffracted from crystalline tin oxide (ICSD = 01-077-2296) of the FTO substrate. The XRD patterns do not show any sort of crystalline impurity peak such as from CaO or any other type of TiO$_2$.

Although, all the films demonstrated similar XRD patterns and thus a similar phase of perovskite CaTiO$_3$ and

anatase TiO_2 in crystalline deposit in each case, however, it is perceived from these XRDs that the degree of crystallinity of $CaTiO_3$ and TiO_2 phases are influenced by the temperature during the deposition. For example, the film deposited at 500 °C, TiO_2 peak situated at 25.2° appears as highest intensity peak while the characteristics $CaTiO_3$ peaks centered at 47.4° and 47.5° remain low and various other peaks are absent. With rise in the deposition temperature the intensity of TiO_2 peak (25.2°) is reduced and $CaTiO_3$ peaks become sharp and various other peaks are quite visible in the film specimen developed at 600 °C.

To confirm this observation, quantitative phase analysis was applied on each XRD pattern and crystalline proportions of perovskite $CaTiO_3$ and anatase TiO_2 phases were measured in each film and are shown in the form of pi-charts (insets of Fig. 3).

The XRD quantitative phase analysis reveals that the film deposited at 500 °C contains higher percentage of crystalline anatase TiO_2 (73%) as compared to perovskite $CaTiO_3$ (27%). The crystalline contents of TiO_2 are observed to decrease with increase in deposition temperature and $CaTiO_3$–TiO_2 composite prepared at 550 °C is poised at 43% of anatase TiO_2 and 57% of perovskite $CaTiO_3$. The crystalline content of anatase TiO_2 further reduces to 17% and perovskite $CaTiO_3$ with 83% becomes as major phase in the crystalline $CaTiO_3$–TiO_2 product obtained at 600 °C. Worth mentioning here is that the films produced at three different temperatures differ in terms of their percentage crystalline composition of the two phases, however, the total crystalline plus non-crystalline phases of $CaTiO_3$:TiO_2 remain at 1:1 ratio and can be further ascertained from elemental (EDX and XPS) analyses of the films. The variation in crystalline contents of the films as a result of change in deposition temperature is a common aspect of AACVD where the reactions between precursor gaseous intermediates and substrate surface are profoundly influenced by the deposition temperature and thus lead to the formation of oxide products with different level of crystalline phases [41, 42].

3.5 SEM/EDX analysis

The surface and cross sectional FESEM images of $CaTiO_3$–TiO_2 composite oxide films developed at 500, 550 and 600 °C are presented in Fig. 4. The low resolution SEM images (Fig. 4a–c) reveal that $CaTiO_3$–TiO_2 crystallites are homogeneously distributed on the substrate surface over all temperature ranges. The high resolution SEM images (Fig. 4a1–c1) unveil the spherical shape of the $CaTiO_3$–TiO_2 crystallites which are regularly connected with each other and it has been observed that size, shape and texture of these spheroids are not significantly altered with increase in deposition temperature from 500 to 600 °C. The average diameter

of the $CaTiO_3$–TiO_2 particles have been measured in the size range of 0.3–1.8 μm.

However, SEM cross sectional views, Fig. 4a2–c2, depict the variation in film thickness as a function of varying substrate temperature. The $CaTiO_3$–TiO_2 film developed at 500 °C displayed a layer of spheroid particles of thickness around 3.0 μm which almost become double (≈ 6.0 μm) when temperature rises to 550 °C, suggesting that film growth rates become better with rise in the deposition temperature. The nucleation and growth of spherical particles further enhances with increasing deposition temperature up to 600 °C. A layer of spheroid objects can be clearly seen on the surface with an average thickness of 9.0 μm.

Energy dispersive X-ray analysis (EDX) is used to confirm the elemental composition and purity of all the composite films. The EDX spectra (supporting information Fig. S1a–c) demonstrate the atomic ratio of Ca to Ti is about 1:2, confirming the formation of 1:1 for $CaTiO_3$:TiO_2 composite material. EDX patterns also indicate a uniform concentration of Ca and Ti in all regions examined, indicating that $CaTiO_3$ and TiO_2 phases are uniformly distributed. The various signals resulted from substrate elements (i.e., Sn, Si, Na, F) and Au-coating are not excluded from EDX spectra. Further the composite nature of $CaTiO_3$–TiO_2 films were established from EDX mapping and results (supporting information Fig. S2a–c) indicate that calcium, titanium and oxygen atoms are evenly distributed throughout the films matrices confirming the composite nature of all films.

3.6 XPS analysis

In order to further confirm the elemental composition and the chemical state of $CaTiO_3$–TiO_2 composite, XPS measurements were carried out on the film fabricated at 600 °C and XPS spectra are illustrated in Fig. 5. The survey spectrum, (Fig. 5a), reveals that Ca, Ti and O are major elements present on the film surface and Ca/Ti atomic ratio was found to be $\approx 1:2$ that is consistent with EDX results. The high resolution XPS spectrum of Ca (Fig. 5b) displays two peaks located at about 346.0 eV and 351.0 eV corresponding to the Ca2p3/2 and Ca2p1/2, respectively and represents the chemical state of Ca^{2+} [43]. The double peak can be de-convoluted from the curve fitting into four sub peaks at 346.3, 347.9, 349.9 and 351.4 eV, Fig. 5b. These results suggest the presence of $CaTiO_3$ (347.9 eV) with some $CaCO_3$ (349.9 eV) and these data are in accordance with reported data for $CaTiO_3$ [44]. The XPS spectrum of Ti shows two main peaks at 458.0 eV and 464.0 eV that can be referred to the Ti 2p3/2 and Ti 2p1/2, respectively, confirming the presence of Ti^{4+} in $CaTiO_3$–TiO_2 composite oxides [45]. In Fig. 5d, the O 1s profile can be fitted to two symmetrical peaks at 529.2 and 529.8 eV, accredited to Ca–O and Ti–O, respectively. The small peaks at 531.1 eV can be assigned
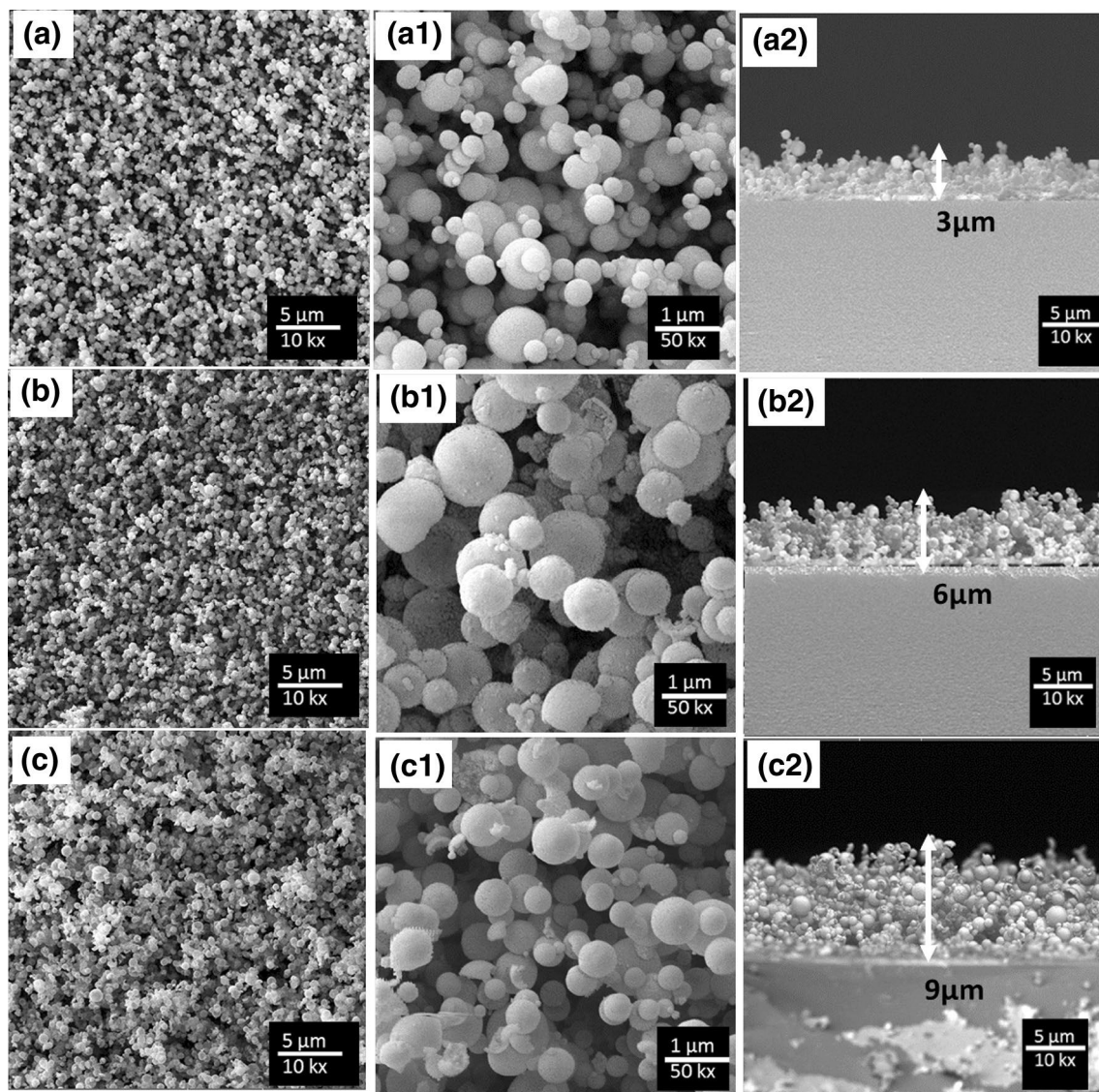
Fig. 4 **a–c** Low resolution (×10k), **a1–c1** high resolution (×50k) surface and **a2–c2** cross sectional FESEM images of $CaTiO_3$–TiO_2 thin films deposited on FTO glass substrates at temperatures **a** 500 °C, **b** 550 °C and **c** 600 °C, respectively

to the chemisorbed oxygen caused by the surface hydroxyl (OH) [28].

3.7 Optical properties

The optical bandgap (E_g) of $CaTiO_3$–TiO_2 composite films grown at 600 °C was investigated by UV–Vis absorption spectrophotometry. UV–Vis absorption spectrum (Fig. 6) of $CaTiO_3$–TiO_2 display a steep absorption in the wavelength region of 300–470 nm. The optical band gap of the composite films has been graphically determined from Tauc's formula valid for direct bandgap semiconductors (i.e., $\alpha h\nu = A(h\nu - E_g)^{1/2}$) where A is a constant, α is the absorption

coefficient, $h\nu$ is the photon energy, and E_g is the band gap energy.

The inset of Fig. 6 shows the corresponding Tauc's plot between $(\alpha h\nu)^2$ versus E_g. A direct band gap value for composite oxide film is derived as 3.0 eV from the extrapolated straight lines to the X axis of E_g at $\alpha = 0$. The bandgaps for perovskite $CaTiO_3$ and anatase TiO_2 are reported to be 3.5 eV and 3.2 eV respectively [46, 47]. The optical measurements of $CaTiO_3$–TiO_2 composite film show that incorporation of TiO_2 into perovskite $CaTiO_3$ leads to a red shift in the optical response and a concomitant reduction of 0.5 eV in E_g of $CaTiO_3$. It is well established that coupling of two semiconductors results in contraction of optical bandgap due to the synergic effect of the two components
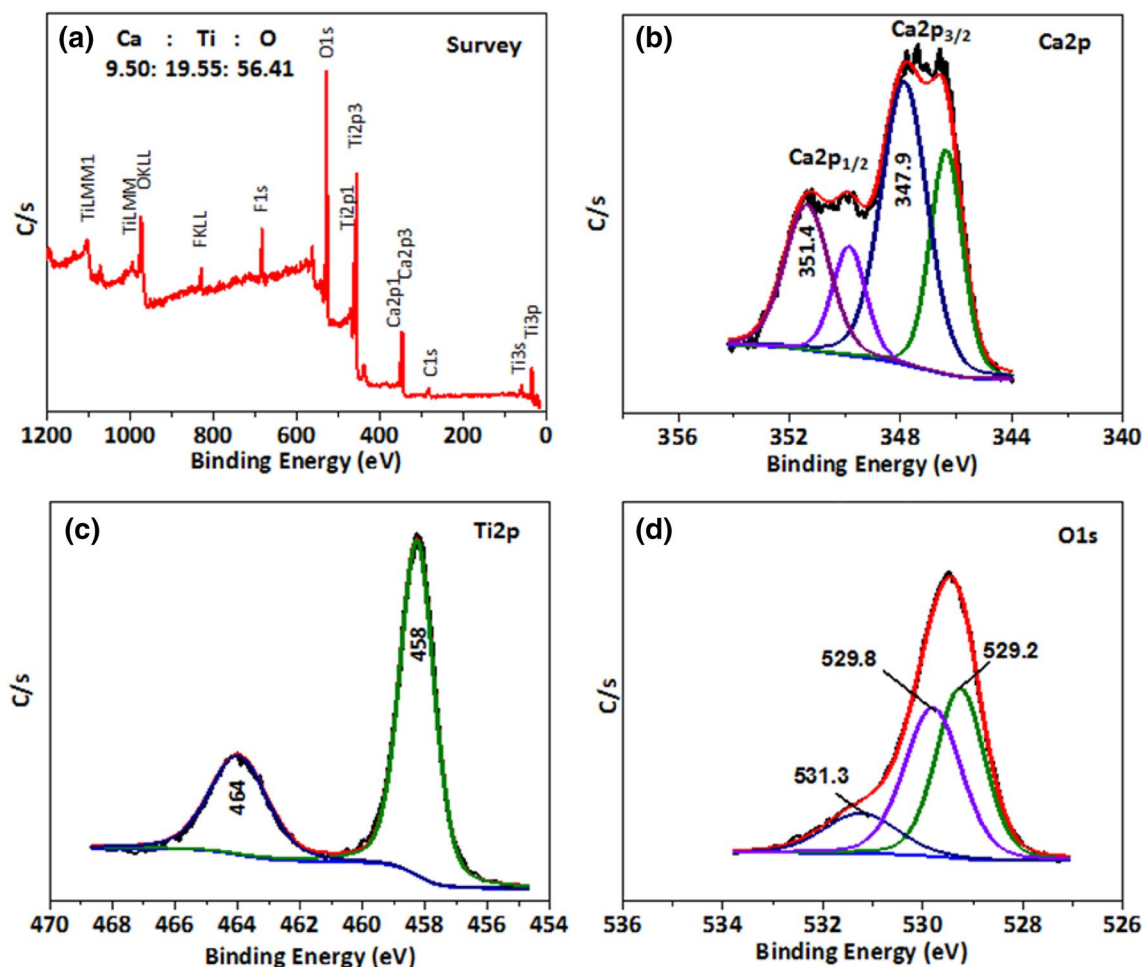
Fig. 5 **a** Survey scan spectrum (XPS) of $CaTiO_3$–TiO_2 composite films prepared at 600 °C; High resolution spectrum of $CaTiO_3$–TiO_2 for **b** Ca 2p, **c** Ti 2p, **d** O 1s
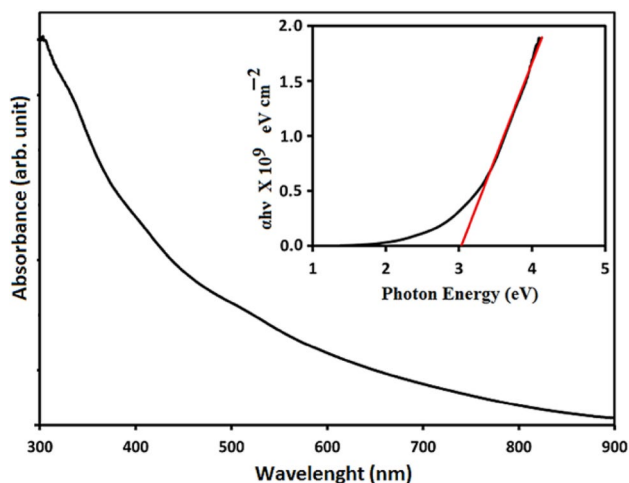

Fig. 6 UV–Vis absorption spectrum of $CaTiO_3$–TiO_2 composite, deposited at 600 °C by AACVD. The inset demonstrates the corresponding Tauc's plot of $(\alpha h\nu)^2$ versus E/eV

present in the composite [48, 49]. The positive effect of synergic cooperation is commonly explained by the opinion that, in the new equilibrium Fermi energy level of the $CaTiO_3$–TiO_2 composite, the photo excited electron on the conduction band of $CaTiO_3$ are readily transferred into the TiO_2 particles. The accumulation of excess electrons in TiO_2 diminishes the recombination of photo-induced electrons and holes and thus, improves the photocatalytic activity of the films. Similar synergistic effects of TiO_2 with $SrTiO_3$ and $BaTiO_3$ have been previously reported for their enhanced photocatalytic efficiencies [50, 51].

3.8 Photoelectrochemical performances

To evaluate the photoelectrochemical (PEC) behavior of the $CaTiO_3$–TiO_2 (CT) composite, the films were employed as photoanodes in a 3-arm cell. A Pt counter electrode and 1 M NaOH as electrolyte were employed, and all $CaTiO_3$–TiO_2 electrodes (CT-500, CT-550 and CT-600) were illuminated

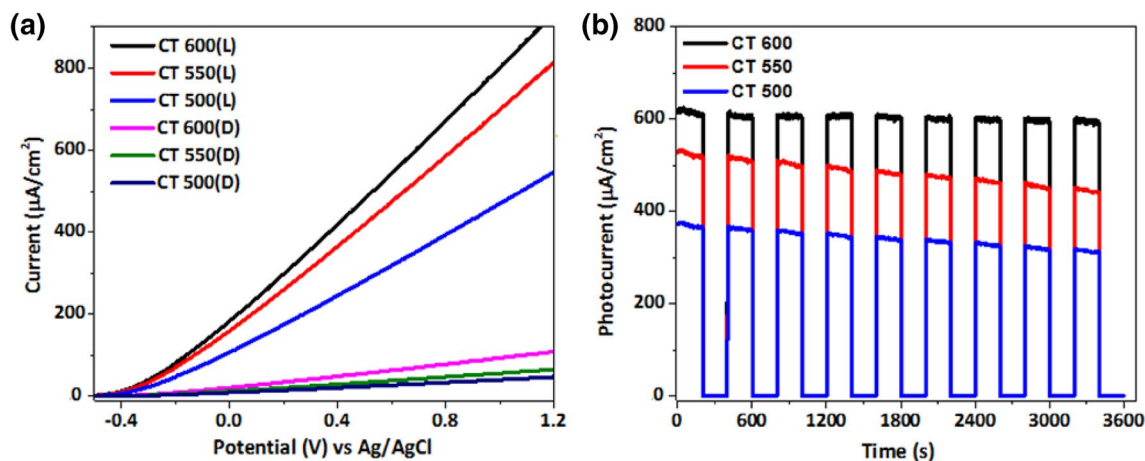**Fig. 7** **a** LSV curves and **b** transient photocurrent responses recorded for $CaTiO_3$–TiO_2 electrodes deposited at 550, 590 and 630 °C in 1 M NaOH under dark and simulated AM 1.5 illumination of 100 mW cm^{-2}

with simulated sunlight, (100 mW xenon lamp equipped with AM 1.5 filters). The current density–voltage (*J–V*) characteristics of $CaTiO_3$–TiO_2 electrodes as recorded in dark (D) and light (L) conditions are shown in Fig. 7a. The dark current coming from each electrode at −0.4 V to +0.7 V (vs. Ag/AgCl) was almost negligible. A prompt photocurrent response in all cases is observed after the illumination, however, the magnitude of photocurrent varied depending upon the deposition temperature. Notably, the CT-600 electrode deposited at 600 °C exhibited highest photocurrent of 610 μA cm^{-2} at 0.7 V compared to the CT-550 and CT-500 electrodes which produced photocurrent densities of 530 and 370 μA cm^{-2}, respectively. This reflects that deposition temperature is a significant factor influencing the photocurrent density of the film electrode which ultimately affects the structural properties of the $CaTiO_3$–TiO_2 electrodes such as crystallinity, surface morphology and thickness. It is evident from XRD and SEM (surface and cross-sectional) results that CT-600 electrode exhibits higher crystallinity and denser layer (~9 μm) of microspherical particles (Fig. 4c2) than the other two electrodes (CT-550 and CT-500) which are relatively less crystalline and thinner (~6 μm and ~3 μm, respectively). The improved crystalline pattern of CT 600 eliminates the distortion and poor lattice mismatching between particle–particle or particle–conducting layer connection and develops better linkage between $CaTiO_3$–TiO_2 crystallites that lead to a reduction in the recombination and improved charge transport properties in the electrode, thus exhibiting better PEC performance. It is well known that the electrode fabrication method has a strong effect on the crystalline structure and morphology of the composite film system and thus the performance of the PEC cells [7].

To further confirm that photoresponses of $CaTiO_3$–TiO_2 electrodes are due to the absorption of light, choronoamperometric I–t studies were carried out under the white light

illumination of 100 mW cm^{-2} with an on–off illumination cycle of 200 s and a bias potential of +0.7 V (vs. Ag/AgCl). Figure 7b illustrates that all $CaTiO_3$–TiO_2 photoanodes were able to sustain and replicate their photocurrents during long term continuous on–off illumination for 1 h without any noticeable deterioration in photocurrent which reveals their excellent stabilities during the photo-induced electrochemical process. Additionally, the transient photocurrent values recoded for CT-500 (372 μA cm^{-2}), CT 550 (527 μA cm^{-2}) and CT-600 (610 μA cm^{-2}) correspond well with their linear sweep voltametry results, thus strengthening the photoelectrocatalytic performance of the $CaTiO_3$–TiO_2 electrodes.

Electrochemical impedance spectroscopy (EIS) was also performed to probe the resistivity of the electrode materials and the interfacial properties between the electrode and the electrolyte over a frequency from 10 kHz to 0.1 Hz in the presence of 0.1 M NaOH. Figure 8a shows the EIS Nyquist plot of $CaTiO_3$–TiO_2 electrodes measured in dark and illumination conditions. In the Nyquist plot, the arc of a semicircle at high frequency range represents the typical charge-transfer process, and the diameter of the semicircle reflects the charge-transfer resistance (R_{ct}).

As shown in Fig. 8a the diameter of all $CaTiO_3$–TiO_2 electrodes was much larger in the dark offering higher R_{ct} which inhibits the charge transfer process across the electrode–electrolyte interface. However in presence of light, the Nyquist curves of all $CaTiO_3$–TiO_2 electrodes are considerably reduced in size, indicating lowering of R_{ct} that facilitate the fast mobility of electron by reducing the recombination of electron–hole pairs. The R_{ct} values measured from Nyquist plots are listed in Table 3. Moreover, the Table 5 compares the R_{ct} values of three CT (L) electrodes and reveals that influence of illumination on CT-600 electrode is more pronounced and results in lowest R_{ct} value representing the efficient rather enhanced charge
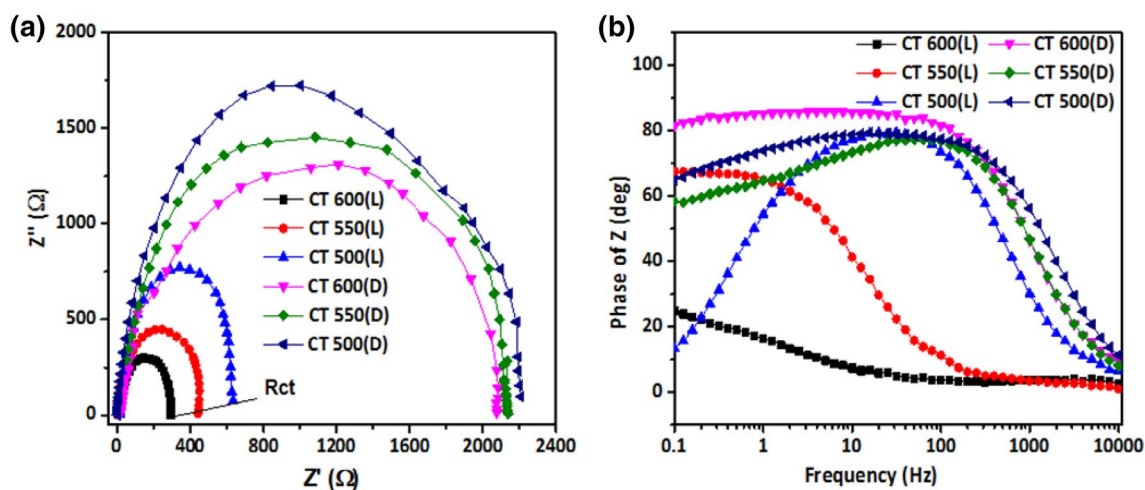
Fig. 8 **a** EIS Nyquist plots and **b** bode phase plots observed for the CaTiO$_3$–TiO$_2$ films fabricated at different temperatures using a frequency range of 0.1 Hz–10 kHz both in dark and light conditions

Table 5 Charge transfer resistance, maximum frequency and recombination lifetime calculated for CaTiO$_3$–TiO$_2$ film electrodes fabricated at different indicated temperatures via AACVD

Film electrode	R_{ct} (ohm)	f_{max} (Hz)	τ_n (ms)
CT 500 (D)	2208	265.4	0.59
CT 500 (L)	442	16.2	9.81
CT 550 (D)	2140	157.6	1.00
CT 550 (L)	442	1.96	81.1
CT 600 (D)	2078	137.9	1.11
CT 600 (L)	295	0.5	318

R_{ct} charge transfer resistance, f_{max} maximum frequency, τ_n recombination lifetime

separation and transfer across the interface. Moreover, it reduces the possibility of charge recombination at the surface of the CT-600 electrode.

Consequently, the EIS findings are completely in agreement with voltammetry results and further endorse the PEC capabilities of CaTiO$_3$–TiO$_2$ electrodes.

The charge-transfer diffusion properties of CaTiO$_3$–TiO$_2$ electrodes can be further established by recording the frequency dependent phase angle plots (Bode plot) in dark and light conditions (Fig. 8b). In presence of light, the characteristic frequency peak (f_{max}) of all CaTiO$_3$–TiO$_2$ films are observed to shift towards low frequency region (0.1 Hz) (Table 3), suggesting the fast and facile electron-transfer behavior of all CT electrodes. Further, the low resistance of CT-600 under light exhibits peak shift more towards the low frequency region in the Bode plot (Table 3; Fig. 8b). Under illumination, the phase angle of the plot at higher frequency is less than 90° and there is lesser log z value in low frequency range of 1–100 Hz. This suggests that the electrode does not behave as an ideal capacitor.

The f_{max} observed for each CaTiO$_3$–TiO$_2$ electrode can be used to determine the electron recombination lifetime (τ_n) using the following equation:

$$\tau_n = {}^1\!/_{2\pi f_{max}}$$

This defines the lifetime of charge carrier inside the bulk of the electrode material and higher τ_n value corresponds to the longer lifespan of the charge carrier. The calculated τ_n values for all CaTiO$_3$–TiO$_2$ electrodes in absence and presence of light are shown in Table 3. The data depicts that the lifetime of charge carriers corresponding to CaTiO$_3$–TiO$_2$ electrodes is prolonged effectively under light compared to dark conditions. The τ_n value is highest as calculated for CT-600 (L) which in turn confirms the production of highest current density in it. Thus, the CaTiO$_3$–TiO$_2$ electrode made at 600 °C shows smaller interface impedance, higher photocurrent density, and better charge transportation properties as compared to the electrodes prepared at 500 and 550 °C.

The PEC results of CaTiO$_3$–TiO$_2$ composite oxide have been compared with other calcium titanate based materials. The photocurrent density of 610 µA cm^{-2} and electrochemical stability of 1 h observed in the current studies is several time higher than the pristine CaTiO$_3$ (1.2 µA cm^{-2}) [52] and Zr-doped CaTiO$_3$ (100 µA cm^{-2}) [28] electrodes. The other Ag–CaTiO$_3$ [44] and CaTiO$_3$–graphene [31] composites were investigated for photocatalysis of organic molecules and are not relevant to the present work. The higher photo-response of CaTiO$_3$–TiO$_2$ composite is attributed to better separation and transportation of photo-induced holes and electrons at the junction and this mechanism is depicted in Fig. 9. The bandgaps of anatase TiO$_2$ (3.2 eV) and perovskite CaTiO$_3$ (3.5 eV) are aligned in such manner that incident UV light can simultaneously activate both
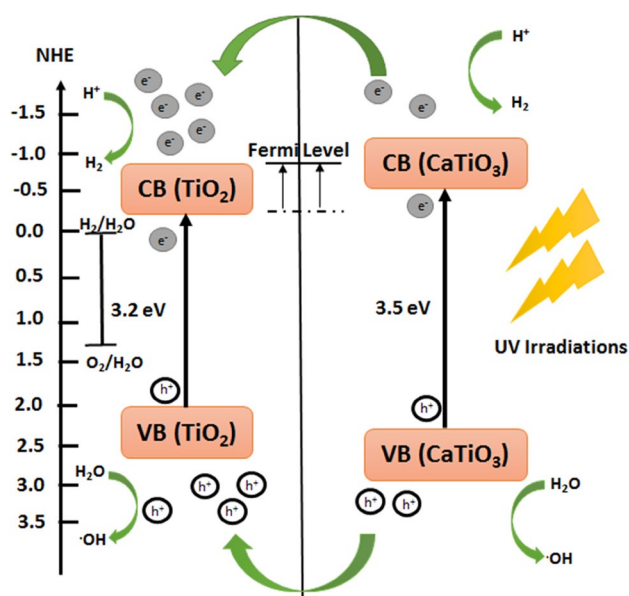
Fig. 9 Schematic representation of band positions and the spatial separation of light generated inter-particle charges during photocatalytic activation of CaTiO₃–TiO₂ with a negative shift in its Fermi level

semiconductor materials. Upon illumination, electrons from VBs of $CaTiO_3$ and TiO_2 are excited and successively promoted to their respective CBs, leaving behind holes. These holes then perform oxidation at semiconductor/electrolyte junction [39]. Since the CB of TiO_2 is ~ 0.3 V more positive [44], the promoted electrons from the CB of $CaTiO_3$ are shifted there. The accumulation of excess electrons in TiO_2 causes a negative shift in its Fermi levels. In a previous photocatalytic investigation based on titanium-oxide-based composite of perovskite like structure, it was argued that the electrons flow to the CB of TiO_2 through a pn-junction. A pn-junction is an interface where the p-type acceptor compound ($CaTiO_3$) and n-type donor compound (TiO_2) connect electronically [53, 54]. The charge flow through the pn-junction may form highly reduced states of $CaTiO_3$–TiO_2 that are stable even under oxygen saturated conditions by inducing an efficient spatial separation of the photogenerated interparticle charges. This in turn improves the photocatalytic water splitting performance [53, 55]. The Fermi levels of the undoped, intrinsic n-type TiO_2 semiconductor lies at the minimum of its CB range. The coupling of $CaTiO_3$ elevates Fermi energy levels to assume a more negative redox potential compared to H^+/H_2 (0 V vs. NHE). Thus an overall higher work function is shown for water reduction reactions [55, 56]. The negative shift in Fermi level is indicative of a large accumulation of electrons at the heterojunctions of TiO_2 and $CaTiO_3$, reflecting a decrease in recombination of charges [57]. For efficient water splitting to produce H_2, the CB level should be sufficiently higher (more negative) than the reduction potential of H_2O. The theoretical minimum bandgap for water splitting has been calculated to be 1.23 eV [58]. It is expected that the $CaTiO_3$–TiO_2 composite can optimize light harvesting abilities with the incorporation of anatase and perovskite crystallites.

4 Conclusions

In the present work, photoelectrochemical water splitting has been demonstrated over robust and stable $CaTiO_3$–TiO_2 composite electrodes which have been developed through solution processed AACVD approach utilizing a mixture of $[Ca_2(TFA)_3(OAc)(^iPrOH)(H_2O)(THF)_3]$ and $Ti((CH_3)_2CHO)_4$ as dual source precursors. It has been found that the incorporation of TiO_2 into perovskite $CaTiO_3$ leads to decrease in the optical bandgap from 3.5 to 3.0 eV while reducing the possibility of e^-–h^+ recombination, thereby enhancing photocatalytic activity. The PEC experiments on $CaTiO_3$–TiO_2 electrodes at 0.7 V versus. Ag/AgCl/3 M KCl under simulated solar irradiation of AM 1.5 G (100 mW cm⁻²) show maximum anodic photocurrent density of 610 μA cm⁻² in 1 M NaOH. This enhanced activity of the composite film fabricated at 600 °C is further supported by EIS results that show a maximum frequency peak below 0.1 Hz. These results demonstrate efficient photocatalytic cleavage of water using novel $CaTiO_3$–TiO_2 composite films prepared through CVD methods. Such unique and efficient composite materials may find application in solar energy harvesting via photoelectrochemical cells.

5 Supplementary data

CCDC 1531480 contains the supplementary crystallographic data for this paper. These data can be obtained free of charge from the Cambridge Crystallographic Data Centre via http://www.ccdc.cam.ac.uk/data_request/cif.

Electronic Supplementary Information (ESI) available: [AT-IR, ¹H-NMR and ¹⁹F-NMR spectra's Energy dispersive X-ray spectra].

References

1. S. Chen, S.S. Thind, A. Chen, Electrochem. Commun. **63**, 10–17 (2016)
2. T. Hisatomi, J. Kubota, K. Domen, Chem. Soc. Rev. **43**, 7520–7535 (2014)
3. X. Zou, Y. Zhang, Chem. Soc. Rev. **44**, 5148–5180 (2015)

4. X. Chen, L. Liu, F. Huang, Chem. Soc. Rev. **44**, 1861–1885 (2015)
5. Y. Ma, X. Wang, Y. Jia, X. Chen, H. Han, C. Li, Chem. Rev. **114**, 9987–10043 (2014)
6. E. Kalamaras, V. Dracopoulos, L. Sygellou, P. Lianos, Chem. Eng. J. **295**, 288–294 (2016)
7. W. Wang, M.O. Tadé, Z. Shao, Chem. Soc. Rev. **44**, 5371–5408 (2015)
8. S.S. Arbuj, R.R. Hawaldar, S. Varma, S.B. Waghmode, B.N. Wani, Sci. Adv. Mater. **4**, 568–572 (2012)
9. N.P. Dasgupta, J. Sun, C. Liu, S. Brittman, S.C. Andrews, J. Lim, H. Gao, R. Yan, P. Yang, Adv. Mater. **26**, 2137–2184 (2014)
10. O.A. Jaramillo-Quintero, M.S. de la Fuente, R.S. Sanchez, I.B. Recalde, E.J. Juarez-Perez, M.E. Rincón, I. Mora-Seró, Nanoscale **8**, 6271–6277 (2016)
11. E. Grabowska, Appl. Catal. B **186**, 97–126 (2016)
12. T.W. Kim, K.-S. Choi, Science **343**, 990–994 (2014)
13. H. Zhang, G. Chen, Y. Li, Y. Teng, Int. J. Hydrogen Energy **35**, 2713–2716 (2010)
14. A. Mumtaz, N.M. Mohamed, M. Mazhar, M.A. Ehsan, M.S. Mohamed, Saheed, ACS Appl. Mater. Interfaces **8**, 9037–9049 (2016)
15. D. Sharma, S. Upadhyay, V.R. Satsangi, R. Shrivastav, U.V. Waghmare, S. Dass, J. Phys. Chem. C **118**, 25320–25329 (2014)
16. W. Yang, Y. Yu, M.B. Starr, X. Yin, Z. Li, A. Kvit, S. Wang, P. Zhao, X. Wang, Nano Lett. **15**, 7574–7580 (2015)
17. K. Shimura, H. Yoshida, Energy Environ. Sci. **3**, 615–617 (2010)
18. A.A. Tahir, H.A. Burch, K.U. Wijayantha, B.G. Pollet, Int. J. Hydrogen Energy **38**, 4315–4323 (2013)
19. A.A. Tahir, M. Mat-Teridi, K. Wijayantha, Phys. Status Solidi Rapid Res. Lett. **8**, 976–981 (2014)
20. M. Mat-Teridi, A.A. Tahir, S. Senthilarasu, K. Wijayantha, M.Y. Sulaiman, N. Ahmad-Ludin, M.A. Ibrahim, K. Sopian, Phys. Status Solidi Rapid Res. Lett. **8**, 982–986 (2014)
21. M.A. Ehsan, H. Khaledi, A. Pandikumar, N.M. Huang, Z. Arifin, M. Mazhar, J. Solid State Chem. **230**, 155–162 (2015)
22. M.A. Mansoor, M.A. Ehsan, V. McKee, N.-M. Huang, M. Ebadi, Z. Arifin, W.J. Basirun, M. Mazhar, J. Mater. Chem. A **1**, 5284–5292 (2013)
23. A.A. Tahir, K.U. Wijayantha, S. Saremi-Yarahmadi, M. Mazhar, V. McKee, Chem. Mater. **21**, 3763–3772 (2009)
24. A.A. Tahir, T. Peiris, K. Wijayantha, Chem. Vap. Depos **18**, 107–111 (2012)
25. M.A. Ehsan, R. Naeem, V. McKee, A.S. Hakeem, M. Mazhar, Sol. Energy Mater Sol. Cells **161**, 328–337 (2017)
26. C. Han, J. Liu, W. Yang, Q. Wu, H. Yang, X. Xue, J. Sol-Gel Sci. Technol. **81**, 806–813 (2017)
27. J. Jang, P. Borse, J.S. Lee, K. Lim, O. Jung, E. Jeong, J. Bae, H. Kim, Bull. Korean Chem. Soc. **32**, 95–99 (2011)
28. X. Huang, Y. Xin, H. Wu, F. Ying, Y. Min, W. Li, S. Wang, Z.-j. Wu, Trans. Nonferr. Metals Soc. China **26**, 464–471 (2016)
29. J. Shi, L. Guo, Prog. Nat. Sci. Mater. **22**, 592–615 (2012)
30. H. Zhang, G. Chen, X. He, J. Xu, J. Alloys Compd. **516**, 91–95 (2012)
31. T. Xian, H. Yang, Y. Huo, Phys. Scr. **89**, 115801 (2014)
32. M. Eghbali-Arani, A. Sobhani-Nasab, M. Rahimi-Nasrabadi, F. Ahmadi, S. Pourmasoud, Ultrason. Sonochem. **43**, 120–135 (2018)
33. S. Pourmasoud, A. Sobhani-Nasab, M. Behpour, M. Rahimi-Nasrabadi, F. Ahmadi, J. Mol. Struct. **1157**, 607–615 (2018)
34. A. Sobhani-Nasab, Z. Zahraei, M. Akbari, M. Maddahfar, S.M. Hosseinpour-Mashkani, J. Mol. Struct. **1139**, 430–435 (2017)
35. C.B. Hübschle, G.M. Sheldrick, B. Dittrich, J. Appl. Crystallogr. **44**, 1281–1284 (2011)
36. G.M. Sheldrick, Acta Crystallogr. A **71**, 3–8 (2015)
37. G.M. Sheldrick, Acta Crystallogr. C **71**, 3–8 (2015)
38. X. Cai, Y. Wu, L. Wang, N. Yan, J. Liu, X. Fang, Y. Fang, Soft Matter. **9**, 5807–5814 (2013)
39. M. Veith, M. Haas, V. Huch, Chem. Mater. **17**, 95–101 (2005)
40. F.H. Allen, Acta Crystallogr. B **58**, 380–388 (2002)
41. M.A. Ehsan, H. Khaledi, A. Pandikumar, P. Rameshkumar, N.M. Huang, Z. Arifin, M. Mazhar, New J. Chem. **39**, 7442–7452 (2015)
42. A.A. Tahir, M.A. Ehsan, M. Mazhar, K.U. Wijayantha, M. Zeller, A. Hunter, Chem. Mater. **22**, 5084–5092 (2010)
43. D. Wei, Y. Zhou, D. Jia, Y. Wang, J. Biomed. Mater. Res. B **84**, 444–451 (2008)
44. S.-W. Lee, L. Lozano-Sánchez, V. Rodríguez-González, J. Hazard. Mater. **263**, 20–27 (2013)
45. D. Boukhvalov, D. Korotin, A. Efremov, E. Kurmaev, C. Borchers, I. Zhidkov, D. Gunderov, R. Valiev, N. Gavrilov, S. Cholakh, Phys. Status Solidi B **252**, 748–754 (2015)
46. H. Mizoguchi, K. Ueda, M. Orita, S.-C. Moon, K. Kajihara, M. Hirano, H. Hosono, Mater. Res. Bull. **37**, 2401–2406 (2002)
47. D.O. Scanlon, C.W. Dunnill, J. Buckeridge, S.A. Shevlin, A.J. Logsdail, S.M. Woodley, C.R.A. Catlow, M.J. Powell, R.G. Palgrave, I.P. Parkin, Nat. Mater. **12**, 798–801 (2013)
48. F. Hu, W. Chen, Electrochem. Commun. **13**, 955–958 (2011)
49. M.A. Mansoor, M. Mazhar, M. Ebadi, H.N. Ming, M.A.M. Teridi, L.K. Mun, New J. Chem. **40**, 5177–5184 (2016)
50. S.E. Stanca, R. Müller, M. Urban, A. Csaki, F. Froehlich, C. Krafft, J. Popp, W. Fritzsche, Catal. Sci. Technol. **2**, 1472–1479 (2012)
51. J. Ng, S. Xu, X. Zhang, H.Y. Yang, D.D. Sun, Adv. Funct. Mater. **20**, 4287–4294 (2010)
52. X. Yan, X. Huang, Y. Fang, Y. Min, Z. Wu, W. Li, J. Yuan, L. Tan, Int. J. Electrochem. Sci. **9**, 5155–5163 (2014)
53. M. Ueda, S. Otsuka-Yao-Matsuo, Sci. Technol. Adv. Mater. **5**, 187–193 (2004)
54. T. Omata, S. Otsuka-Yao-Matsuo, J. Photochem. Photobiol. **156**, 243–248 (2003)
55. Z. Jin, X. Zhang, Y. Li, S. Li, G. Lu, Catal. Commun. **8**, 1267–1273 (2007)
56. A. Kudo, Y. Miseki, Chem. Soc. Rev. **38**, 253–278 (2009)
57. J. Zhang, J.H. Bang, C. Tang, P.V. Kamat, ACS Nano **4**, 387–395 (2009)
58. A. Kudo, H. Kato, I. Tsuji, Chem. Lett. **33**, 1534–1539 (2004)